Influence of Metal–Graphene Contact on the Operation and Scalability of Graphene Field-Effect Transistors

Pei Zhao, *Student Member, IEEE*, Qin Zhang, *Member, IEEE*, Debdeep Jena, and Siyuranga O. Koswatta

Abstract—We explore the effects of metal contacts on the operation and scalability of 2-D graphene field-effect transistors (GFETs) using detailed numerical device simulations based on the nonequilibrium Green's function formalism self-consistently solved with the Poisson equation at the ballistic limit. Our treatment of metal–graphene (M–G) contacts captures the following: 1) the doping effect due to the shift of the Fermi level in graphene contacts and 2) the density-of-states (DOS) broadening effect inside graphene contacts due to metal-induced states (MIS). Our results confirm the asymmetric transfer characteristics in GFETs due to the doping effect by metal contacts. Furthermore, at higher M–G coupling strengths, the contact DOS broadening effect increases the on-current, while the impact on the minimum current ($I_{\min}$) in the OFF-state depends on the source-to-drain bias voltage and the work-function difference between graphene and the contact metal. Interestingly, with scaling of the channel length, the MIS inside the channel has a weak influence on $I_{\min}$ even at large M–G coupling strengths, while direct source-to-drain (S → D) tunneling has a stronger influence. Therefore, channel length scalability of GFETs with sufficient gate control will be mainly limited by direct S → D tunneling, and not by the MIS.

Index Terms—Density-of-states (DOS) broadening, graphene field-effect transistors (GFETs), metal-induced states (MIS), source-to-drain (S → D) tunneling.

I. INTRODUCTION

GRAPHENE is a 2-D zero-bandgap material with carbon atoms arranged in a honeycomb lattice [1], [2]. A finite bandgap can be obtained through quantum confinement by cutting 2-D graphene into strips as graphene nanoribbons (GNRs). High-quality GNRs with acceptable edge uniformity, however, pose a technological challenge. However, monolayer 2-D graphene can be achieved by means of mechanical exfoliation of graphite, high-temperature sublimation of silicon from SiC substrates [3], or CVD growth on metal substrates [4], [5]. Although 2-D monolayer graphene lacks a bandgap, it still shows promising potential for applications in high-frequency devices that do not require a high on/off ratio as demanded by digital logic [6]–[10]. Recently, many theoretical and experimental works have studied the microscopic physics of metal–graphene (M–G) contacts, which show that metal contacts could play a critical role on the device performance [11]–[22]. In this regard, theoretical studies based on the density functional theory show that, when graphene is covered by a metal electrode, the Fermi level of graphene underneath will be shifted [11], [12]. This behavior has also been observed in experiments [13], [14]. However, the detailed influence of M–G contacts on the transport properties and, more importantly, on the scalability of graphene field-effect transistors (GFETs) has not been addressed yet.

In this paper, we study the effect of M–G coupling on the operation and the scalability of 2-D GFETs. Even though previous simulation studies have explained the asymmetric transport characteristics in electrostatically doped graphene p-n junctions [23], experiments have indicated that M–G contacts themselves may also lead to asymmetric conduction in 2-D GFETs [13], [14]. In this paper, we confirm the latter observation by using a self-consistent 2-D electrostatic solution of the GFET geometry [24] which captures the metal-induced doping effect. M–G coupling could also lead to metal-induced states (MIS) inside the graphene channel, which is similar in origin to the metal-induced gap states in conventional metal–semiconductor contacts [25]. Experiments have also confirmed that the impact of metal contacts on the channel potential extends into the channel for several hundred nanometers [20]–[22]. Here, we consider the influence of MIS on the scalability of GFETs and provide detailed insights into the impact of metal contacts on GFET characteristics.

II. DEVICE MODEL AND THE SIMULATION APPROACH

The modeled device is shown in Fig. 1. The channel is assumed to be uniform graphene with a width W of 150 nm. At $W = 150$ nm, the current density (in milliamperes per micrometer) is similar to the 2-D analytical result, which justifies the effective 2-D limit of the modeled GFET. The top gate insulator is $t_{ox} = 1.5$ nm thick and has a dielectric constant $\varepsilon_{ox} = 20$. With such excellent dielectric assumptions, short-channel effects can be avoided in our model, and we can focus
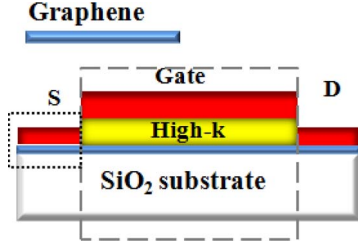
Fig. 1. Structure of modeled device. The graphene channel is fully covered by the top gate. $t_{ox} = 1.5$ nm and $\varepsilon_{ox} = 20$. The SiO$_2$ substrate is 50 nm thick and is connected to ground. This dielectric assumption can avoid short-channel effects, and it is used as the nominal condition.

on the effects from the M–G contacts (the impact of the oxide thickness will be discussed hereinafter). The SiO$_2$ substrate is 50 nm in thickness and connected to the ground. The simulated area is only the channel region (dashed rectangle in Fig. 1) with fixed boundary conditions at the source and the drain. The electrostatic solution procedure is described in [24]. The effective oxide thickness (EOT) of our modeled device is only 0.3 nm; thus, the quantum capacitance (C_Q) corresponding to the graphene density of states (DOS) cannot be ignored. Our simulations self-constantly solve both the transport and the electrostatic parts; thus, the effect of quantum capacitance is naturally captured. In other words, the total gate capacitance C_G is not simply equal to C_{ox} but more generally to $C_G = (C_{ox}C_Q)/(C_{ox} + C_Q)$.

Here, the tight-binding model for ballistic transport in the channel is assumed, and it is solved using a mode-space-based nonequilibrium Green's function formalism [26]. The mode-space approach significantly reduces the computational cost while still maintaining the accuracy, as has already been demonstrated in simulations of MOSFET [27], carbon nanotube FET [28], and GNR FET [29]. In our calculations, we assume that the potential variation along the channel width direction is negligible. Based on this approximation, the electrostatics is solved in 2-D, and the mode-space method yields accurate results.

In this paper, the contact regions are assumed to be semi-infinitely long and comprised of a metal layer deposited on top of the graphene layer [11], [16]. In this M–G hybrid system (dotted rectangle in Fig. 1), the Fermi level of the graphene underneath is shifted, and the DOS is broadened due to the M–G coupling [11], [12]. The Fermi level shift in the contact regions is modeled by $\Delta E_{contact} = E_F - E_{Dirac}$, where E_F ($E_F = 0$ eV) is the Fermi level and E_{Dirac} is the Dirac point inside the graphene contact regions. The broadening of DOS is captured by a phenomenological approach [15]–[18] with an M–G coupling strength of Δ (in millielectronvolts) that can reproduce the *ab initio* simulation results [17]. The effect of M–G contacts on the channel region is captured through a contact self-energy function $\Sigma_{S,D} = \tau g_S \tau^\dagger$, where τ is the

coupling matrix between the contact and the channel ($\tau^\dagger$ is its Hermitian conjugate) and g_S is the surface Green's function of the contact, $g_S(E) = [(E + i\Delta)I - H_{contact}]^{-1}$ [16]. Here, $H_{contact}$ is the contact Hamiltonian matrix, and I is the identity matrix. In the mode-space approach, g_S of the qth mode can be analytically expressed as the equation of g_{sq} shown at the bottom of the page. The source contact self-energy function for the qth mode is $\Sigma_{Sq}^{1,1} = (b_{1q})^2 g_{sq}$, where $b_{1q} = t_0$ and $b_{2q} = 2t_0 \cos(q\pi/(n + 1))$ are the coupling parameters in the qth mode 1-D sublattice, t_0 is the nearest neighbor tight-binding parameter, n is the number of carbon atoms in the width direction, and U_1 is the electrostatic potential at the source end [29]. A similar expression applies for the drain contact self-energy function Σ_{Dq}, with U_1 being replaced by the potential at the drain end. The retarded Green's function for qth mode is then determined by $G_q(E) = [(E + i0^+)I - H_q - \Sigma_{Sq} - \Sigma_{Dq}]^{-1}$, where H_q is the channel Hamiltonian matrix for the qth mode

$$[H_q] = \begin{bmatrix} U_1 & b_{2q} & & \\ b_{2q} & U_2 & b_{1q} & \\ & b_{1q} & U_3 & b_{2q} \\ & & \cdots & \cdots \end{bmatrix}.$$

Here, U_i is the electrostatic potential at the ith atom in the qth mode. The source (drain) local DOS (LDOS) within the channel are computed as $LDOS_{S(D)} = G_q \Gamma_{S(D)} G_q^\dagger/2\pi$, where $\Gamma_{S(D)} = i(\Sigma_{S(D)} - \Sigma_{S(D)}^+)$ is the energy broadening due to the source (drain) contact. The total LDOS within the channel is given by the summation of $LDOS_S$ and $LDOS_D$. Finally, the channel current is computed from $I_{DS} = (2e/h) \int T(E)(f_S(E) - f_D(E))dE$, where $f_{S/D}$ are the source/drain Fermi–Dirac distribution functions, respectively, and $T(E) = \sum_q T_q(E)$ is the total transmission coefficient with T_q being the transmission of the qth mode.

III. EFFECT OF M–G CONTACT ON THE CHANNEL

To explore the influence of M–G contact on the channel, we plot the energy-position-resolved channel LDOS in logarithmic scale in Fig. 2 for (a) $\Delta = 0$ meV and (b) $\Delta = 50$ meV. The device structure is the same as shown in Fig. 1 with $V_{DS} = 0$ V and $V_{GS} = 0.1$ V. The potential profiles of the channel Dirac point (dashed lines) are the self-consistent results. The channel Dirac point at the source and drain ends are equal to 0.2 eV, which shows the p-type doping effect inside the contact with $\Delta E_{contact} = -0.2$ eV. When $\Delta = 0$ meV, LDOS near the contact Dirac point energy level (0.2 eV) is very low (darker color). As mentioned in Section II, states within the channel are given by $LDOS_{S(D)} = G_q \Gamma_{S(D)} G_q^\dagger/2\pi$. When $\Delta = 0$ meV, the contact broadening effect $\Gamma_{S(D)} \approx 0$ leads to a negligible broadening of the channel states. Even though states do exist within the channel, those states with infinitesimal

$$g_{sq} = \frac{(E - U_1 + i\Delta)^2 + b_{1q}^2 - b_{2q}^2 + \sqrt{\left[(E - U_1 + i\Delta)^2 + b_{1q}^2 - b_{2q}^2\right]^2 - 4(E - U_1 + i\Delta)^2 b_{1q}^2}}{2b_{1q}^2(E - U_1 + i\Delta)}$$
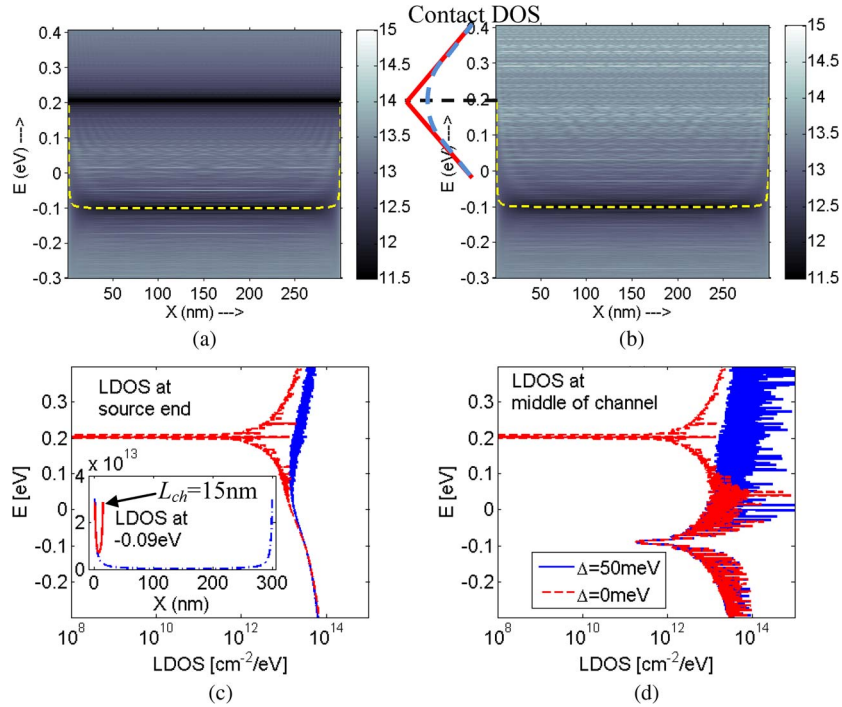
Fig. 2. Energy-position-resolved channel LDOS at $V_{DS} = 0$ V and $V_G = 0.1$ V, $\Delta E_{contact} = -0.2$ eV. (a) When $\Delta = 0$ meV, LDOS along the contact Dirac point at 0.2 eV are unobservable due to a contact which induced a negligible broadening when $\Gamma_{S(D)} \approx 0$. (b) When $\Delta = 50$ meV, the broadening effect $\Gamma_{S(D)}$ is large, and then, the states near 0.2 eV are broadened and can be observed. LDOS versus energy plot (c) at source end of the channel and (d) at middle of the channel for different Δ. Inset figure shows the channel LDOS at -0.09 eV, comparing with $L_{ch} = 300$, when $L_{ch} = 15$ nm LDOS along the channel increase due to contact-induced states.

broadening are not visible in the energy-position-resolved LDOS. However, when $\Delta = 50$ meV, $\Gamma_{S(D)}$ is large, which gives obvious broadening effect of the channel states. Thus, energy-position-resolved LDOS clearly shows states near the energy level of the contact Dirac point in Fig. 2(b). Near the gate-controlled channel Dirac point at about -0.09 eV, *contact-induced evanescent states* can be observed penetrating into the channel. Those states originate from the wave functions incident from the contacts. Because graphene has a zero bandgap, those evanescent states can penetrate for a long distance.

Fig. 2(c) and (d) show LDOS versus energy at the source end of the channel and at the middle of the channel for two Δ values. It is clear that, at $\Delta = 0$ meV, a negligible $\Gamma_{S(D)}$ will lead to unobservable states at the energy level of the contact Dirac point. M–G coupling can broaden the zero DOS near the contact Dirac point, but the effect of broadening is weak if the intrinsic graphene DOS is large [sketch of intrinsic DOS solid line and broadened DOS dashed line in Fig. 2(b)]. Along the channel Dirac point at around -0.09 eV, the MIS inside the channel is negligible; thus, LDOS does not have a dependence on Δ. Contact-induced evanescent states will affect the channel LDOS, but the effect of MIS due to M–G coupling Δ is trivial. Golizadeh–Mojarad's work [15] shows that, without any bias, the contact Dirac point is at the same energy level as the channel Dirac point. MIS along the channel Dirac point shows strong dependence on M–G coupling Δ. This conclusion is valid if no bias is added and contact Fermi level is fixed at the Dirac point. Our work provides a complete description since the metal-induced contact doping effect is captured, and the potential profile is solved self-consistently at any given bias.

The calculated LDOS inside the channel is the summation of the intrinsic graphene DOS and states due to contact incident wave-function penetration. The inset of Fig. 2(c) shows that, at $L_{ch} = 15$ nm, contact incident wave functions increase the channel LDOS, which has a large influence on the minimum current as discussed later.

IV. RESULTS AND DISCUSSION

Fig. 3 shows the calculated transfer characteristics ($T = 300$ K) at low drain bias $V_{DS} = 0.1$ V with different Fermi level alignments $\Delta E_{contact}$ in the contact regions. The M–G coupling strength is taken to be $\Delta = 50$ meV. The effects of different Δ's are discussed later. If $\Delta E_{contact} = 0$ eV, graphene contact is not doped by metal, and the transfer curve is symmetric as shown in Fig. 3(a). The minimum conduction point is located at gate voltage $V_G = V_{DS}/2$. In Fig. 3(b), $\Delta E_{contact} = -0.2$ eV (p-type doping), a typical value for Au contact is based on [11]. At negative V_G, carriers can directly go through the channel. At positive V_G, the electrons need to go through the channel Dirac point (see schematic potential of the Dirac point). Because DOS near the Dirac point is very low, it suppresses the carrier injection from contact to channel. Thus, the positive current branch is reduced compared to the negative branch. The complete transfer curve shows a clear asymmetric behavior. We point out that the gate voltage at which the minimum conduction point occurs is also slightly shifted due to the asymmetric barriers at the contacts. When $\Delta E_{contact}$ is positive as in Fig. 3(c), an effective n-type doping is introduced by the metal contacts. A similar asymmetric behavior with the
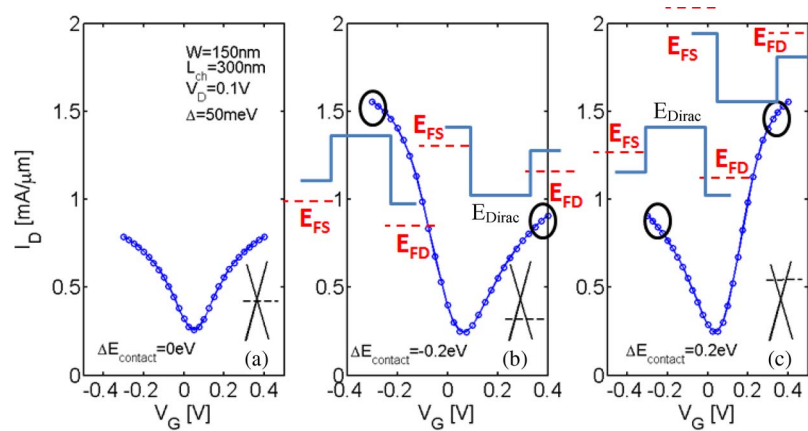
Fig. 3. Transfer characteristics under different $\Delta E_{\text{contact}}$. (a) Without any shift of Fermi level in the contact region, symmetric transfer characteristics can be seen. When the Fermi level of contact regions of graphene is shifted due to the metal contact as shown in (b) $\Delta E_{\text{contact}} = -0.2$ eV and (c) $\Delta E_{\text{contact}} = 0.2$ eV, asymmetric transfer characteristics are observed.

positive current branch being greater than the negative branch is seen in that case. Another interesting feature is, compared with I_{DS}–V_{GS} in Fig. 3(a), a contact doping effect that increases the on-current as shown in Fig. 3(b) and (c).

The effect of different coupling strengths Δ's at $V_{\text{DS}} = 0.1$ V is shown in Fig. 4. The rigorous explanation of the values used for Δ is related to the M–G hybrid system, which is beyond the focus of this work (see [11] and [12] for details). For a comparison, we define three Δ values here; $\Delta = 0$ eV for the intrinsic graphene, $\Delta = 8$ meV for weak M–G coupling, and $\Delta = 50$ meV for strong coupling. Fig. 4(a) and (b) shows the transfer characteristics at channel length $L_{\text{ch}} = 300$ and 15 nm, respectively. We observe that the on-current *increases* for larger Δ, which can be understood by looking at the impact of Δ on $T(E)$ in the ON-state (Fig. 4(c), center panel). First of all, it is seen that, at $\Delta = 0$ eV, there are three distinct minimum points in $T(E)$ corresponding to the zero-DOS Dirac point position inside the channel, source, and drain regions, respectively. On the other hand, at larger Δ, $T(E)$ near the source and the drain Dirac points increases due to metal-induced DOS broadening inside the M–G contact regions, which ultimately enhances the current transport (Fig. 4(c), right panel). Interestingly, the minimum current I_{min}, however, does not show a dependence on Δ. Fig. 4(d) shows the potential profiles of the Dirac point (left), $T(E)$ (center), and the energy-resolved current density $J(E)$ (right) at the minimum conduction point of $L_{\text{ch}} = 15$ nm device. Although the DOS of the graphene contact is broadened by the metal contact, $T(E)$ in the *current-carrying* energy window between the source Fermi level E_{FS} and the drain Fermi level E_{FD} remains the same for different Δ values. At $L_{\text{ch}} = 15$ nm, *direct* source-to-drain (S → D) tunneling is the dominant factor controlling I_{min}. Furthermore, it is necessary to point out that the aforementioned interesting features due to various Δ's still remain valid with other oxide thickness and dielectric values, since the aforementioned effects are mainly due to contact DOS broadening. Here, transfer characteristics with $t_{\text{ox}} = 5$ nm, $\varepsilon_{\text{ox}} = 9$, and $\Delta = 50$ meV (solid lines) are shown in order to compare different EOT values. When EOT increases, the current decreases. The current reduction is due to the loss of C_G and longer effective electrostatic scaling length at larger

EOT [24]. At large positive and negative V_{GS}, C_Q is large, and since $C_G = (C_{\text{ox}}C_Q)/(C_{\text{ox}} + C_Q)$, C_G is dominated by C_{ox}. When EOT increases, C_{ox} decreases; thus, the loss of C_G is the main reason leading to current reduction. On the other hand, at small V_{GS}, C_Q is small and dominant. The drop in C_G is small, and longer effective electrostatic scaling length further limits the current. In addition, when EOT increases, the longer effective electrostatic scaling length increases the asymmetry in the I_{DS}–V_{GS} characteristics. Short-channel effects can also be observed with large EOT. At $L_{\text{ch}} = 15$ nm, the minimum conduction point shifts about 0.15 V, while at $L_{\text{ch}} = 300$ nm, such shifts are very small.

Fig. 5(a) and (b) shows a comparison of the effect of different coupling strengths Δ's at large $V_{\text{DS}} = 0.3$ V. When $\Delta = 0$ eV, in addition to the primary minimum conduction point, a distortion appears in the I_D–V_{GS} characteristics. The two minima are due to the misalignment of the Dirac point of the channel and drain regions. With $V_{\text{DS}} = 0.3$ V, the drain Dirac point locates between E_{FS} and E_{FD}. The channel Dirac point is controlled by the gate. At $V_{G1} = -0.05$ V, all carriers pass through the channel hole cone, and at $V_{G2} = 0.1$ V, carriers move through the channel electron cone. However, at $V_G = 0.025$ V, both electron and hole cones are involved; thus, the channel Dirac point leads to a local minimum. When $\Delta = 50$ meV, DOS near the contact Dirac point are broadened. The only minimum conduction point is due to the channel Dirac point, and the distortion disappears. A recent experimental work reports the presence of this type of distortion before annealing and the disappearance of the distortion after annealing [30]. Our model explains this behavior without resorting to new postulates (such as charge depinning at metal contacts as proposed in [30]). Before annealing, the M–G interface is not clean, and the coupling is weak. After annealing, better M–G coupling is achieved, and the distortion disappears. In contrast to the low-V_{DS} case in Fig. 4, I_{min} at large V_{DS} shows a dependence on Δ. Fig. 5(d) shows the internal transport properties near the minimum conduction point of $L_{\text{ch}} = 15$ nm GFET. In this case, at large V_{DS}, the Dirac point in the drain region is located between E_{FS} and E_{FD}. The broadened DOS in the drain contact at larger Δ increases $J(E)$ and, thus, the I_{min}
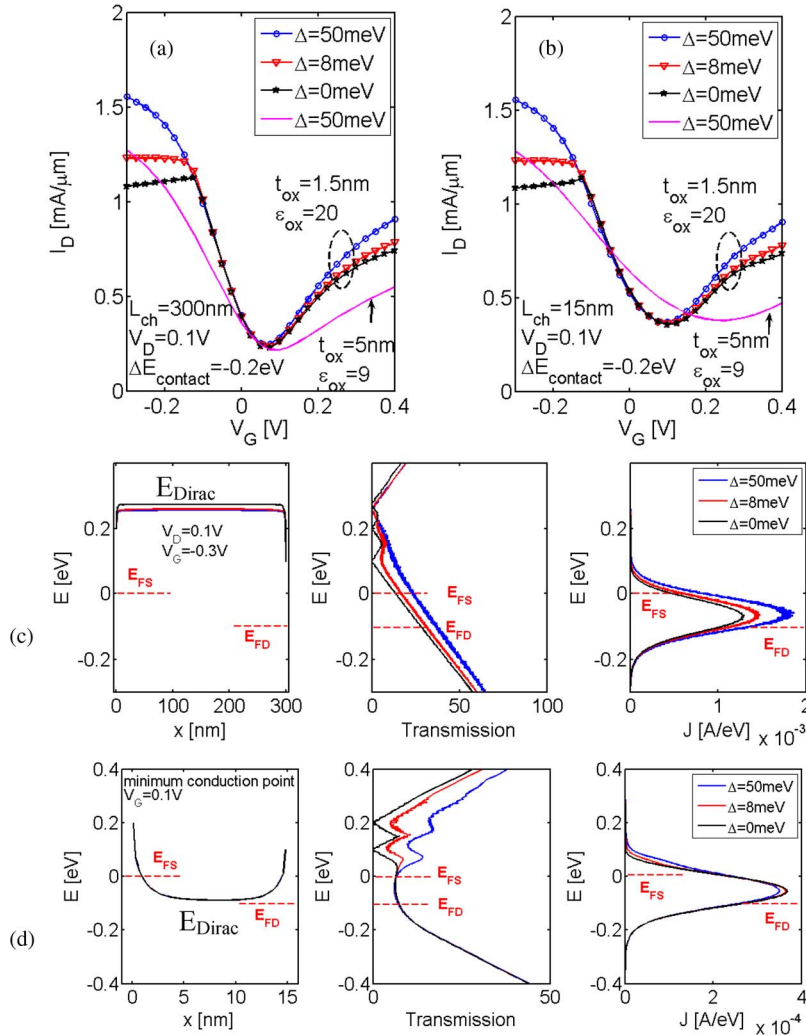
Fig. 4. Effect of different coupling strength Δ at $V_{\mathrm{DS}} = 0.1$ V. On-current increases at larger Δ for both (a) $L_{\mathrm{ch}} = 300$ nm and (b) $L_{\mathrm{ch}} = 15$ nm. The solid lines are the transfer characteristics with $t_{\mathrm{ox}} = 5$ nm, $\varepsilon_{\mathrm{ox}} = 9$, and $\Delta = 50$ meV. When EOT increases, the minimum conduction point shifts due to the short-channel effect. (c) Increase of on-current corresponds to the broadened DOS of the graphene contact. However, I_{min} does not change with Δ even at $L_{\mathrm{ch}} = 15$ nm. (d) $T(E)$ between E_{FS} and E_{FD} does not depend on Δ, suggesting that direct S $\rightarrow$ D tunneling is the dominant factor.

does as well. On the other hand, $T(E)$ near the channel Dirac point energy at about -0.3 eV *does not* show a dependence on Δ. Thus, the increase in I_{min} can be attributed to the DOS broadening in the contacts. Here, we point out that the "large-V_{DS}" condition is determined by $|V_{\mathrm{DS}}| > |(E_F - E_D)/q|$ that would increase I_{min} at larger Δ values.

The performance of GFETs upon scaling of the channel length is crucial for technology scaling, which is discussed in Fig. 6. Our model assumes a high-k insulator to obtain superior electrostatic gate control to avoid the short-channel effect. In Fig. 6, $\Delta = 50$ meV, and I_{on} remains almost the same for different channel lengths, but I_{min} increases at short L_{ch}. At short channel lengths, I_{min} is mainly affected by direct S $\rightarrow$ D tunneling. Here, when L_{ch} is reduced from 150 to 40 nm, because the probability for S $\rightarrow$ D tunneling rises, I_{min} increases by about 10%. When $L_{\mathrm{ch}} = 15$ nm, S $\rightarrow$ D tunneling becomes more severe, and I_{min} increases by 1.5 times compared with $L_{\mathrm{ch}} = 150$ nm. A similar scaling behavior persists even at $V_{\mathrm{DS}} = 0.3$ V, and I_{min} increases by 20% when the channel length shrinks from 150 to 15 nm (not shown).

The I_D versus V_{DS} characteristics are shown in Fig. 7 for (a) $V_{\mathrm{GS}} > 0$ V and (b) $V_{\mathrm{GS}} \leq 0$ V. $\Delta E_{\mathrm{contact}} = 0.5$ eV is assumed as a degenerate n-type contact. The I_{DS}–V_{DS} characteristics at $V_{\mathrm{GS}} = 0.2$ V and $V_{\mathrm{GS}} = 0.4$ V in Fig. 7(a) show a kink characteristic due to an ambipolar channel, which is also observed in the experiments [6]. In the unipolar regime, where $V_{\mathrm{DS}} < V_{\mathrm{DS,kink}}$, the GFET shows saturating characteristics [6]. With $V_{\mathrm{GS}} > 0$ V, the source/channel/drain are all n-type and comprise an n-n-n-type structure, electrons will directly transport through the channel, and, thus, the dependence of the contact DOS and M–G coupling strength Δ is small. With $V_{\mathrm{GS}} \leq 0$ V in (b), at weak coupling as $\Delta = 0$ meV, a saturation behavior has been observed. The reason for this saturation behavior is because $V_{\mathrm{GS}} \leq 0$ V leads to a p-type channel and an n-p-n-type structure, and the n-type contact needs to inject electrons into the channel. When $\Delta = 0$ meV, low-contact DOS near the Dirac point limits the carrier injection from the contacts. With large Δ, contact DOS is broadened, and the saturation behavior disappears, which is similar to large Δ increasing the on-current in Fig. 5.
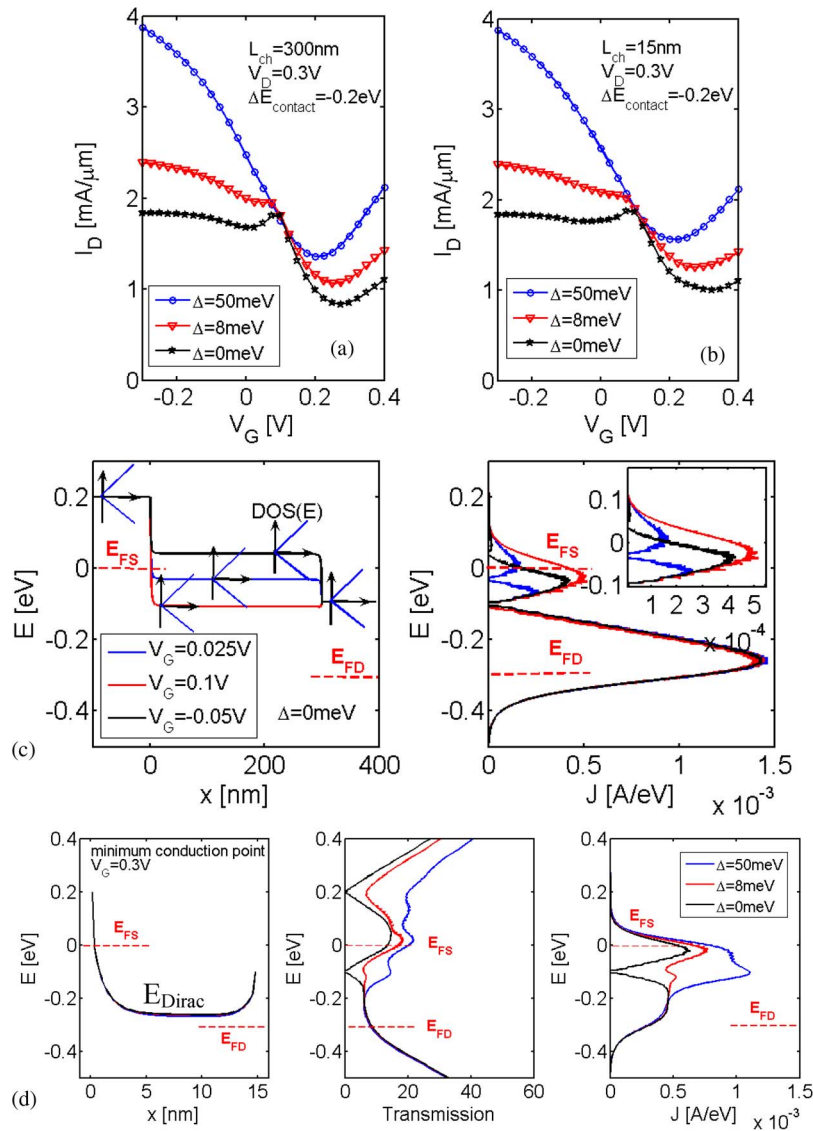
Fig. 5. Effect of different coupling strength Δ at $V_{DS} = 0.3$ V. Aside from the minimum conduction point at about 0.2 V, a distortion appears when (triangle) $\Delta = 8$ meV and (pentagram) $\Delta = 0$ meV. Considering intrinsic graphene, (c) shows the source, drain, and the channel DOS (cartoon) in series which decide how the total carriers transport through the channel. When electron and hole cones are both involved in the transport at $V_G = 0.025$ V, a local minimum is given. As Δ increases, the DOS of graphene contact are broadened, and distortion disappears. (d) For $L_{ch} = 15$ nm at the minimum conduction point $V_G = 0.3$ V, the drain Dirac point is located between E_{FS} and E_{FD}; large Δ broadens the DOS at the drain contact, increasing the $T(E)$ and I_{min}.

Finally, we want to discuss the device performance optimization considering the influence of M–G contact. In Fig. 5, we point out that the broadening of DOS in contacts will increase the I_{min} at large V_{DS}. Thus, to avoid I_{min} current increase due to DOS broadening, the drain bias needs to satisfy $|V_{DS}| < |(E_F - E_D)/q|$. On-current is benefited from strong M–G coupling as shown in Fig. 4. We have also explored the dependence on different $\Delta E_{contact}$ (not shown). If $|\Delta E_{contact}|$ is large, the metal-induced doping effect becomes stronger, the on-current will increase, and I_{min} can be controlled with appropriate V_{DS}. Metals with large work-function difference compared to graphene could be a good candidate to provide large $|\Delta E_{contact}|$ values [11], [12]. The other important issue is that the gate electrostatics play a crucial role. With only the back gate, very long band bending length (long effective electrostatic scaling length) near the contacts has been experimentally

observed [20]–[22]. Our simulation here is based on excellent top gate electrostatics; thus, the band bending length is small, which helps to control the I_{min} while increasing the on-current.

A recent paper has explored the performance of 2-D GFETs under ballistic limits [31]. In [31], the contact self-energy is assumed to be constant and independent of energy, which is a good approximation when a metal destroys the linear dispersion of graphene [11]. Our model uses a different approach to describe the contact, where the contact self-energy depends on the coupling strength Δ. Using Δ as a variable parameter, additional interesting effects have been discussed in this paper. When Δ is small, the linear dispersion of graphene still exists [11], [17]. If the coupling strength Δ further increases to about 0.3 eV, the graphene contact will become metallic-like, and we can also obtain similar results as the pure metal contact case [18].
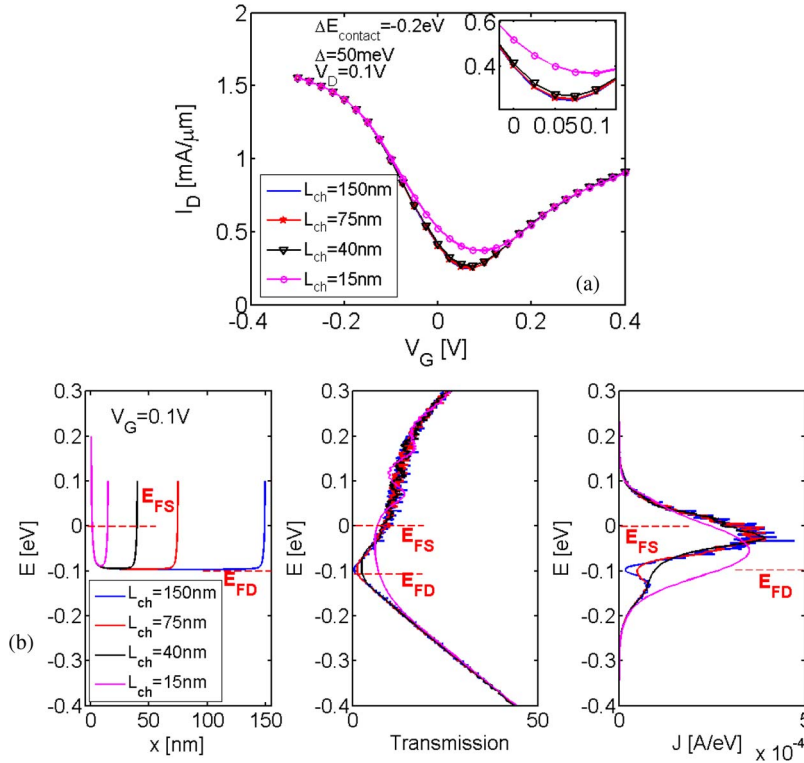
Fig. 6. Effect of channel length scaling at $V_{DS} = 0.1$ V. A high-k insulator is used to avoid the short-channel effect. I_{on} stays the same when L_{ch} is scaled down. As L_{ch} is reduced from 150 to 40 nm, I_{min} increases by 10% due to the direct S → D tunneling. When $L_{ch} = 15$ nm, direct S → D tunneling becomes more severe, and I_{min} increases by about 1.5 times.
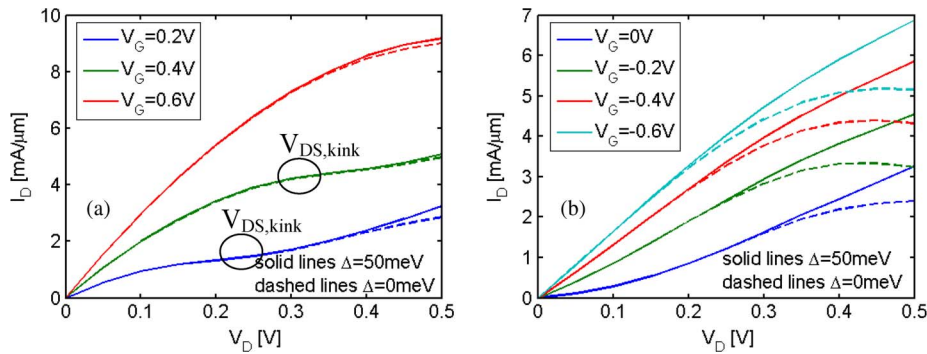

Fig. 7. Effect of coupling strength Δ on the I_{DS} versus V_{DS} characteristics. $\Delta E_{contact} = 0.5$ eV as the heavily doped n-type contact, and $L_{ch} = 100$ nm. The I_D versus V_D is grouped into two areas: (a) $V_{GS} > 0$ V and (b) $V_{GS} \leq 0$ V. (a) shows a kink characteristics with the saturation region due to an ambipolar channel. Influence of Δ is small. With $V_G \leq 0$ V in (b), with weak coupling as $\Delta = 0$ meV, the saturation behavior has been captured. With large Δ, the saturation behavior disappears.

V. CONCLUSION

In this paper, we have used detailed numerical simulations to investigate the impact of metal contacts on the operation of GFETs with electrostatically well-designed top gates. The metal contacts introduce two effects: 1) The Fermi level of graphene underneath the metal is shifted, resulting in asymmetric transfer characteristics, and 2) the DOS of graphene inside the contacts is broadened. Δ is introduced to describe the broadening of the DOS inside the M–G contacts. Based on our results, a weak coupling of metal contacts can cause a distortion of the transfer characteristics, which disappears at strong coupling strengths. Large Δ broadens the contact DOS and increases the I_{on} but does not affect I_{min} at low V_{DS}. At large V_{DS}, i.e., $|V_{DS}| > |(E_F - E_D)/q|$, DOS broadening (MIS inside the contacts) increases both I_{on} and I_{min}. With scaling of channel length, direct S → D tunneling is the crucial factor that increases I_{min} at short channel lengths.

REFERENCES

[1] K. S. Novoselov, A. K. Geim, S. V. Morozov, D. Jiang, M. I. Katsnelson, I. V. Grigorieva, S. V. Dubonos, and A. A. Firsov, "Two-dimensional gas of massless Dirac fermions in graphene," *Nature*, vol. 438, no. 7065, pp. 197–200, Nov. 2005.

[2] Y. Zhang, J. W. Tan, H. L. Stormer, and P. Kim, "Experimental observation of the quantum Hall effect and Berry's phase in graphene," *Nature*, vol. 438, no. 7065, pp. 201–204, Nov. 2005.

[3] C. Berger, Z. Song, X. Li, X. Wu, N. Brown, C. Naud, D. Mayou, T. Li, J. Hass, A. N. Marchenkov, E. H. Conrad, P. N. First, and W. A. de Heer, "Electronic confinement and coherence in patterned epitaxial graphene," *Science*, vol. 312, no. 5777, pp. 1191–1196, May 2006.

[4] X. Li, W. Cai, J. An, S. Kim, J. Nah, D. Yang, R. Piner, A. Velamakanni, I. Jung, E. Tutuc, S. K. Banerjee, L. Colombo, and R. S. Ruoff, "Large-area synthesis of high-quality and uniform graphene films on copper foils," *Science*, vol. 324, no. 5932, pp. 1312–1314, Jun. 2009.

[5] A. Reina, X. Jia, J. Ho, D. Nezich, H. Son, V. Bulovic, M. S. Dresselhaus, and J. Kong, "Large area, few-layer graphene films on arbitrary substrates by chemical vapor deposition," *Nano Lett.*, vol. 9, no. 1, pp. 30–35, 2009.

[6] I. Meric, M. Y. Han, A. F. Young, B. Ozyilmaz, P. Kim, and K. L. Shepard, "Current saturation in zero-bandgap, top-gated graphene field-effect transistors," *Nat. Nanotechnol.*, vol. 3, no. 11, pp. 654–659, Nov. 2008.

[7] Y. M. Lin, K. A. Jenkins, A. Valdes-Garcia, J. P. Small, D. B. Farmer, and P. Avouris, "Operation of graphene transistors at gigahertz frequencies," *Nano Lett.*, vol. 9, no. 1, pp. 422–426, Jan. 2009.

[8] J. S. Moon, D. Curtis, M. Hu, D. Wong, C. McGuire, P. M. Campbell, G. Jernigan, J. T. Tedesco, B. VanMil, R. Myers-Ward, C. Eddy, and D. K. Gaskill, "Epitaxial-graphene RF field-effect transistors on Si-face 6H-SiC substrates," *IEEE Electron Device Lett.*, vol. 30, no. 6, pp. 650–652, Jun. 2009.

[9] M. Y. Lin, K. Jenkins, D. B. Farmer, A. Valdes-Garcia, P. Avouris, C. Y. Sung, H.-Y. Chiu, and B. Ek, "Development of graphene FETs for high frequency electronics," in *IEDM Tech. Dig.*, 2009, pp. 1–4.

[10] Y. M. Lin, C. Dimitrakopoulos, K. A. Jenkins, D. B. Farmer, H. Y. Chiu, A. Grill, and P. Avouris, "100-GHz transistors from wafer-scale epitaxial graphene," *Science*, vol. 327, no. 5966, p. 662, Feb. 2010.

[11] G. Giovannetti, P. A. Khomyakov, G. Brocks, V. M. Karpan, J. van den Brink, and P. J. Kelly, "Doping graphene with metal contacts," *Phys. Rev. Lett.*, vol. 101, no. 2, p. 026 803, Jul. 2008.

[12] P. A. Khomyakov, G. Giovannetti, P. C. Rusu, G. Brocks, J. van den Brink, and P. J. Kelly, "First-principles study of the interaction and charge transfer between graphene and metals," *Phys. Rev. B, Condens. Matter*, vol. 79, no. 19, p. 195 425, May 2009.

[13] B. Huard, N. Stander, J. A. Sulpizio, and D. Goldhaber-Gordon, "Evidence of the role of contacts on the observed electron-hole asymmetry in graphene," *Phys. Rev. B, Condens. Matter*, vol. 78, no. 12, p. 121 402(R), Sep. 2008.

[14] K. Nagashio, T. Nishimura, K. Kita, and A. Toriumi, "Metal/graphene contact as a performance killer of ultra-high mobility graphene—Analysis of intrinsic mobility and contact resistance," in *IEDM Tech. Dig.*, 2009, pp. 1–4.

[15] R. Golizadeh-Mojarad and S. Datta, "Effect of contact induced states on minimum conductivity in graphene," *Phys. Rev. B, Condens. Matter*, vol. 79, no. 8, p. 085 410, Feb. 2009.

[16] N. Nemec, D. Tomanek, and G. Cuniberti, "Modeling extended contacts for nanotube and graphene devices," *Phys. Rev. B, Condens. Matter*, vol. 77, no. 12, p. 125 420, Mar. 2008.

[17] S. Barraza-Lopez, M. Vanević, M. Kindermann, and M. Y. Chou, "Effects of metallic contacts on electron transport through graphene," *Phys. Rev. Lett.*, vol. 104, no. 7, p. 076 807, Feb. 2010.

[18] V. Nam Do and P. Dollfus, "Modelling of metal–graphene coupling and its influence on transport properties in graphene at the charge neutrality point," *J. Phys. Condens. Matter*, vol. 22, no. 42, p. 425 301, Oct. 2010.

[19] D. B. Farmer, R. Golizadeh-Mojarad, V. Perebeinos, Y. M. Lin, G. S. Tulevski, J. C. Tsang, and P. Avouris, "Chemical doping and electron-hole conduction asymmetry in graphene devices," *Nano Lett.*, vol. 9, no. 1, pp. 388–392, Jan. 2009.

[20] E. J. H. Lee, K. Balasubramanian, R. T. Weitz, M. Burghard, and K. Kern, "Contact and edge effects in graphene devices," *Nat. Nanotechnol.*, vol. 3, no. 8, pp. 486–490, Aug. 2008.

[21] F. Xia, T. Mueller, R. Golizadeh-Mojarad, M. Freitag, Y. M. Lin, J. Tsang, V. Perebeinos, and P. Avouris, "Photocurrent imaging and efficient photon detection in a graphene transistor," *Nano Lett.*, vol. 9, no. 3, pp. 1039–1044, 2009.

[22] T. Mueller, F. Xia, M. Freitag, J. Tsang, and P. Avouris, "Role of contacts in graphene transistors: A scanning photocurrent study," *Phys. Rev. B, Condens. Matter*, vol. 79, no. 24, p. 245 430, Jun. 2009.

[23] T. Low, S. Hong, J. Appenzeller, S. Datta, and M. Lundstrom, "Conductance asymmetry of graphene pn junction," *IEEE Trans. Electron Devices*, vol. 56, no. 6, pp. 1292–1299, Jun. 2009.

[24] Q. Zhang, Y. Lu, H. Xing, S. Koester, and S. O. Koswatta, "Scalability of atomic-thin-body (ATB) transistors based on graphene nanoribbons," *IEEE Electron Device Lett.*, vol. 31, no. 6, pp. 531–533, Jun. 2010.

[25] J. Tersoff, "Schottky barrier heights and the continuum of gap states," *Phys. Rev. Lett.*, vol. 52, no. 6, pp. 465–468, Feb. 1984.

[26] S. Datta, *Quantum Transport: Atom to Transistor*. Cambridge, U.K.: Cambridge Univ. Press, 2005.

[27] R. Venugopal, Z. Ren, S. Datta, M. Lundstrom, and D. Jovanovic, "Simulating quantum transport in nanoscale transistors: Real versus mo de-space approaches," *J. Appl. Phys.*, vol. 92, no. 7, pp. 3730–3739, Oct. 2002.

[28] J. Guo, S. Datta, M. Lundstrom, and M. P. Anantram, "Multi-scale modeling of carbon nanotube transistors," *Int. J. Multiscale Comput. Eng.*, vol. 2, no. 2, pp. 257–278, 2004.

[29] P. Zhao and J. Guo, "Modeling edge effects in graphene nanoribbon field-effect transistors with real and mode space methods," *J. Appl. Phys.*, vol. 105, no. 3, p. 034 503, Feb. 2009.

[30] R. Nouchi and K. Tanigaki, "Charge-density depinning at metal contacts of graphene field-effect transistors," *Appl. Phys. Lett.*, vol. 96, no. 25, p. 253 503, Jun. 2010.

[31] J. Chauhan and J. Guo, Assessment of high-frequency performance limits of graphene field-effect transistors, arXiv:1102.1457v1.
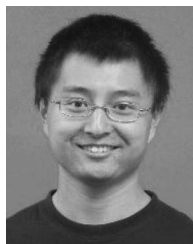
Pei Zhao (S'08) received the B.S. degree in electronic engineering from Huazhong University of Science and Technology, Wuhan, China, in 2007 and the M.S. degree in electrical and computer engineering from the University of Florida, Gainesville, in 2009. He is currently working toward the Ph.D. degree in electrical engineering at the University of Notre Dame, Notre Dame, IN.

His current research work focuses on device physics, modeling, and fabrication of nanoscale transistor.

Qin Zhang (M'09) received the B.S. degree in electronic engineering from Tsinghua University, Beijing, China, in 2003 and the M.S. and Ph.D. degrees in electrical engineering from the University of Notre Dame, Notre Dame, IN, in 2005 and 2009, respectively.

As a recipient of the NIST/MIND Postdoctoral Fellowship, she is currently with the Semiconductor Electronics Division, NIST, Gaithersburg, MD. Her research interests include tunneling devices and graphene electronics.

Debdeep Jena received the B.Tech. degree with a major in electrical engineering and a minor in physics from the Indian Institute of Technology, Kanpur, India, in 1998 and the Ph.D. degree in electrical and computer engineering from the University of California, Santa Barbara, in 2003.

Since 2003, he has been with the faculty of the Department of Electrical Engineering, University of Notre Dame, Notre Dame, IN. His research and teaching interests are in the MBE growth and device applications of quantum semiconductor heterostructures (currently III–V nitride semiconductors), investigation of charge transport in nanostructured semiconducting materials such as graphene, nanowires, and nanocrystals, and their device applications, and in the theory of charge, heat, and spin transport in nanomaterials.

Siyuranga O. Koswatta received the B.S. degree in computer engineering (*summa cum laude*) from the University of Bridgeport, Bridgeport, CT, in 2002 and the M.S. and Ph.D. degrees in electrical and computer engineering from Purdue University, West Lafayette, IN, in 2004 and 2008, respectively.

Since 2008, he has been with the IBM T. J. Watson Research Center, Yorktown Heights, NY, as a Research Staff Member. From 2009 to 2010, he was with the University of Notre Dame, Notre Dame, IN, as the IBM assignee to the Midwest Institute for Nanoelectronics Discovery (MIND). His research interests include modeling and simulation of exploratory devices for nanoelectronic applications. He has been investigating band-to-band-tunneling-based transistors for low-power electronics and carbon-nanotube- and graphene-based low-dimensional devices.